scientific reports

Check for updates

OPEN

Cholesterol depletion suppresses thermal necrosis resistance by alleviating an increase in membrane fluidity

Taisei Kanamori[1], Shogo Yasuda[1], Runjing Duan[1], Mei Ohashi[1], Mai Amou[1], Kanato Hori[1], Ryota Tsuda[1], Taiki Fujimoto[2], Kenjirou Higashi[2], Wei Xu[3], Takuro Niidome[3] & Hiroto Hatakeyama[1]✉

Thermally resistant cancer cells suppress the therapeutic effects of hyperthermia. However, the mechanism underlying the thermal resistance remains unclear. With the aim of enhancing the therapeutic effects of hyperthermia, we investigated the mechanism underlying thermal resistance. We found that heat shock-induced cell death can be classified into two types: late-phase apoptosis and early-phase necrosis. Cell death was suppressed in thermally resistant cells. In addition, heat-induced necrosis resistance correlated with plasma membrane fluidity, which was maintained by cholesterol. Depletion of cholesterol from cancer cells and tumor tissues enhanced the effect of hyperthermia under both in vivo and in vitro conditions. Hence, the findings demonstrate the usefulness of cholesterol as a marker for thermally resistant cancer cells. Furthermore, the combination of cholesterol depletion and hyperthermia may be a new therapeutic strategy for thermally resistant cancers.

Cancer tissues are more vulnerable to heat stress than normal tissues because of their high rate of vascular neogenesis and immature blood vessels[1]. In normal tissues, mature blood vessels can dissipate heat via blood flow. However, tumor tissues possess thin blood vessels and low heat-dissipation capacity, resulting in heat accumulation in the tissue. Hence, tumor tissues are hypothesized to be more vulnerable to heat than normal tissues. Hyperthermia is a novel cancer treatment that induces cell death by applying heat shock to cancer tissues, resulting in the activation of anticancer immune reactions via the release of damage-associated molecular patterns (DAMPs)[2–4]. Although a hyperthermia-based therapeutic approach has been applied in clinical settings, such as in hyperthermic intraperitoneal chemotherapy (HIPEC)[5], it has not become a standard treatment due to its unstable therapeutic effect. Even cancer cell lines derived from the same organ respond differently to heat shock. Furthermore, cancer cell lines demonstrating thermal resistance, i.e., those that are less likely to die by heat shock, have been reported. Hence, thermal resistance may reduce the effect of hyperthermia[6,7]. However, thermal resistance in cancer cells remains incompletely understood.

Heat-shock-induced cell death can be divided into two major types: necrosis and apoptosis[8–10]. Heat-induced apoptosis is driven by intrinsic signals, such as endoplasmic reticulum stress[4,9,11] and mitochondrial damage[12–14], and is mediated by the activation of caspases, leading to chromatin aggregation, DNA fragmentation, and the formation of apoptotic bodies[15]. Activation of these cell death signals is known to occur 3 ~ 6 h after exposure to stress or stimuli[11,13,16]. We have previously reported that metabolic adaptation is likely to suppress apoptosis in thermally resistant cells[6,7]. In cancer cells, lactate fermentation predominates over oxidative phosphorylation for ATP production, even under aerobic conditions, due to the Warburg effect[17,18]. The glycolysis-lactate fermentation pathway is suppressed, and the activation of mitochondrial respiration is selectively activated in thermally resistant cancer cells after heat shock. Under heat shock, protein aggregation induces stress on the endoplasmic reticulum and mitochondria[11,12]. Heat shock proteins (HSPs) are known to be a conserved heat stress response mechanism in various species and inhibit the activation of cell death signals by refolding aggregated proteins[19]. Protein refolding consumes ATP, resulting in energy stress. In contrast, lactate fermentation, a predominant ATP-producing pathway in cancer cells, is accompanied by heat generation, which may rather lead to heat stress

[1]Laboratory of Clinical Pharmacology and Pharmacometrics, Graduate School of Pharmaceutical Sciences, Chiba University, Chiba 260-0856, Japan. [2]Laboratory of Pharmaceutical Technology, Graduate School of Pharmaceutical Sciences, Chiba University, Chiba 260-0856, Japan. [3]Faculty of Advanced Science and Technology, Graduate School of Science and Technology, Kumamoto University, Kumamoto 860-8555, Japan. ✉email: h-hatakeyama@chiba-u.jp

under heat shock. Therefore, under heat shock, metabolic adaptation to ATP production by mitochondria is considered to both suppress heat production and mitigate energy stress in thermally resistant cells.

In contrast, necrosis is a form of cell death that is caused by physical damage to the cell under stress, resulting in structural disruption[8,20]. This structural disruption is directly induced by physical stress and is not considered to be signal-mediated cell death like apoptosis. In cancer hyperthermia, apoptosis and necrosis exhibit differences in terms of therapeutic effects of hyperthermia, such as variances in the ability to release DAMPs[3,21]. Few studies have examined the regulation of these two types of cell death in thermally resistant cancer cells. Particularly, the regulation of necrosis in thermally resistant cancer cells remains unclear. Hence, in this study, we aimed to compare A2780, a thermosensitive cell line, with SKOV3, a thermotolerant cell line to elucidate the mechanism underlying the regulation of necrosis. This is a novel study that aimed to comprehensively evaluate thermally resistant and thermosensitive cells for death-related cellular morphology after heat shock. The rationale was to provide insights into heat-induced necrosis resistance in cells and a novel therapeutic strategy for cancer hyperthermia.

Results

Thermal-resistant cells suppressed apoptosis and necrosis induced by heat shock

To explore the effects of heat-induced necrosis and apoptosis on thermal resistance, we performed flow cytometric analysis of cell death morphology and time course using Annexin and DAPI staining (Fig. 1a). We sorted living and dead cells by gating (Supplementary Fig. S1a-c). Application of heat shock for 1 h at 46°C induced cell death in both A2780 and SKOV3 cells. We defined annexin (-) and DAPI(-) cells as living cells, annexin(+) and DAPI(-) cells as apoptotic cells, and annexin(+) and DAPI(+) cells as necrotic cells. Although the ratio of apoptotic cells increased over time in both A2780 and SKOV3 cells, A2780 cells exhibited a five-fold higher ratio of apoptotic cells than SKOV3 cells at 24 h (Fig. 1b). In contrast, the ratio of necrotic cells increased significantly after heat shock and did not change until 24 h (Fig. 1c). Similar to the results of apoptotic cell death, A2780 cells were susceptible to necrotic cell death. Immediately after the heat shock, the A2780 group showed a three-fold higher ratio of necrotic cells compared to the SKOV3 group. In SKOV3 cells, apoptotic and necrotic cell death induced by heat shock was suppressed compared to that in A2780 cells. The mechanism of how SKOV3 cells suppressed necrotic cell death by heat shock was unclear. Therefore, we examined the mechanism by which SKOV3 cells evade necrotic cell death.

Heat-induced increase in membrane fluidity correlates with necrosis

We hypothesized that an excessive increase in membrane fluidity under conditions involving heat shock would disrupt the membrane structure, resulting in necrotic cell death, which is normally suppressed by cholesterol. Therefore, to confirm whether membrane fluidity is involved in necrotic cell death resistance induced by heat shock, we evaluated the cholesterol levels in A2780 and SKOV3 cells (Fig. 2a). SKOV3 cells showed higher levels of cellular cholesterol than A2780 cells, implying that necrotic death in SKOV3 cells was difficult because of the low temperature-induced increase in membrane fluidity. Next, we evaluated cell viability under several temperatures (Fig. 2b). In addition, we examined whether the observed cell death was specifically associated with necrosis using cell death inhibitors, such as disulfiram (pyroptosis inhibitor), ferrostatin-1 (ferroptosis inhibitor), and GSK872 (necroptosis inhibitor) (Fig. 2c). In these experiments, it was clear that cell death induced immediately after heat shock was necrosis, and SKOV3 cells showed better suppression of necrosis than A2780 cells, even at higher temperatures. To verify the effect of temperature on membrane fluidity, we examined the membrane fluidity of A2780 and SKOV3 cells after heat shock for 1 h at the indicated temperatures (Fig. 2d). Although membrane fluidity at the cell surface was low under 37 °C conditions, regions with high membrane fluidity were partially developed on the cell surface as the temperature increased. Upon treatment of cells at 46 °C for 1 h, necrosis was induced (Fig. 2b), and an increase in membrane fluidity was observed in only A2780 cells (Fig. 2e). No increase in membrane fluidity was observed in SKOV3 cells (Fig. 2e). In contrast, at 50 °C for 1 h, where necrosis was induced in both cells (Fig. 2b), an increase in membrane fluidity was observed in both cells. These results suggest that cholesterol-rich SKOV3 cells may be less susceptible to necrosis than A2780 cells because of the suppression of heat-induced increase in membrane fluidity.

Cholesterol depletion suppresses necrosis resistance by alleviating heat-induced increase in membrane fluidity

To confirm the effect of the cholesterol on membrane fluidity and survival ratio, we measured the survival ratio of A2780 and SKOV3 cells after heat shock with or without cholesterol depletion (Fig. 3a). Both cell lines were heated for 1 h at the indicated temperatures. Under cholesterol-depleted conditions, both cells showed lower cholesterol levels than those under non-cholesterol-depleted conditions (Fig. 3b). To perform a quantitative evaluation, lethal temperature 50 (LT50) values, indicators of necrosis resistance, were calculated based on survival ratios (Fig. 3c). Upon cholesterol depletion, A2780 cells and SKOV3 cells showed lower LT50 values than non-cholesterol-depleted cells at various temperatures. As in the case of non-cholesterol-depleted cells, we evaluated whether necrosis was induced by inhibitors of cell death (Fig. 3d). Cell death, which was enhanced by cholesterol depletion, also resulted in necrosis. Next, to confirm whether cholesterol depletion improved the increase in membrane fluidity caused by heat shock, we observed membrane fluidity after heat shock with or without cholesterol depletion at indicated temperatures (Fig. 3e). The mean membrane fluidity was calculated based on microscopic images (Fig. 3f). At 37 °C, no differences were observed between groups with or without cholesterol depletion. However, a higher degree of increase in fluidity was observed at 46 °C in both cell types (Fig. 3f). Under this condition, membrane fluidity increased further beyond that observed at 50 °C (Fig. 2e). Validation using DMPC/cholesterol liposomes suggested that the MβCD depleted the cholesterol and eliminate lipid rafts in the cell membrane. MβCD may induce the development of a membrane structure that is prone
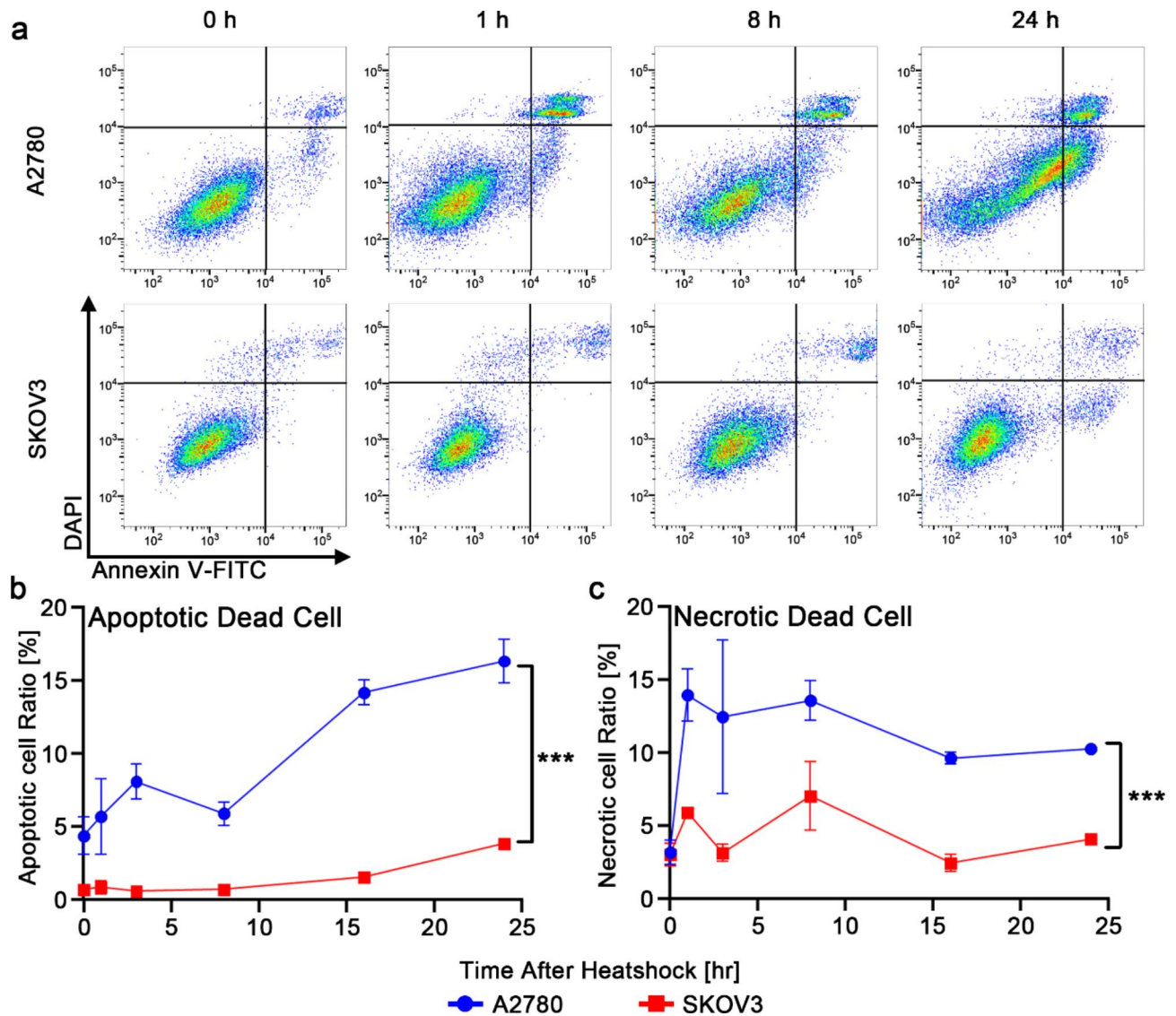
Fig. 1. Analysis of cell death morphology after heat shock. (**a**) Density plot of Annexin-DAPI method after the heat shock up to 24 h. A2780 and SKOV3 cells were heated for 1 h at 46°C, and cell death patterns were analyzed at 0 (non-heated), 1, 3, 8, 16, 24 h. (**b** and **c**) Time profiles of apoptotic and necrotic cells treated with heat shock. The blue and red lines represent the results of A2780 and SKOV3 cells, respectively. Mean ± S.D.; $n = 3 \sim 4$. Student's t-test. ***$P < 0.001$.

to a temperature-dependent increase in membrane fluidity. (Supplementary Fig. S2). The distribution plot of membrane fluidity and the survival ratio immediately after heat shock showed a correlation, indicating that cholesterol-controlled membrane fluidity was involved in necrosis resistance (Fig. 3g).

An increase in membrane fluidity induced by cholesterol depletion improves membrane disruption by heat shock

A correlation between membrane fluidity and necrosis has been described by the aforementioned results. However, whether increased membrane fluidity rendered the membranes more prone to collapse under heat shock conditions remains unclear. Therefore, to confirm membrane disruption, we observed the cell death morphology by real-time imaging of A2780 and SKOV3 cells under heat shock (Fig. 4a-d). We monitored nuclear and cellular calcium in living cells at 46 °C for 1 h. During heat shock, the temperature in the medium was maintained at 46 ~ 46.5 °C (Supplementary Fig. S3a). Only A2780 cells showed complete disappearance of calcium under non-cholesterol-depleted conditions (Fig. 4a and f). Simultaneously, a significant decrease in nuclear fluorescence was observed in the same cells (Fig. 4a and e). These events indicate calcium leakage from the cytosol due to cell membrane disruption and DNA leakage from the nucleus due to the loss of nuclear membrane integrity. In contrast, SKOV3 cells did not exhibit this morphology (Fig. 4b, g, and h). We defined necrotic morphology as complete calcium disappearance due to cell membrane disruption and nuclear fluorescence decay due to the loss of nuclear membrane integrity. Simultaneously, a gradual decrease in calcium levels and an increase in
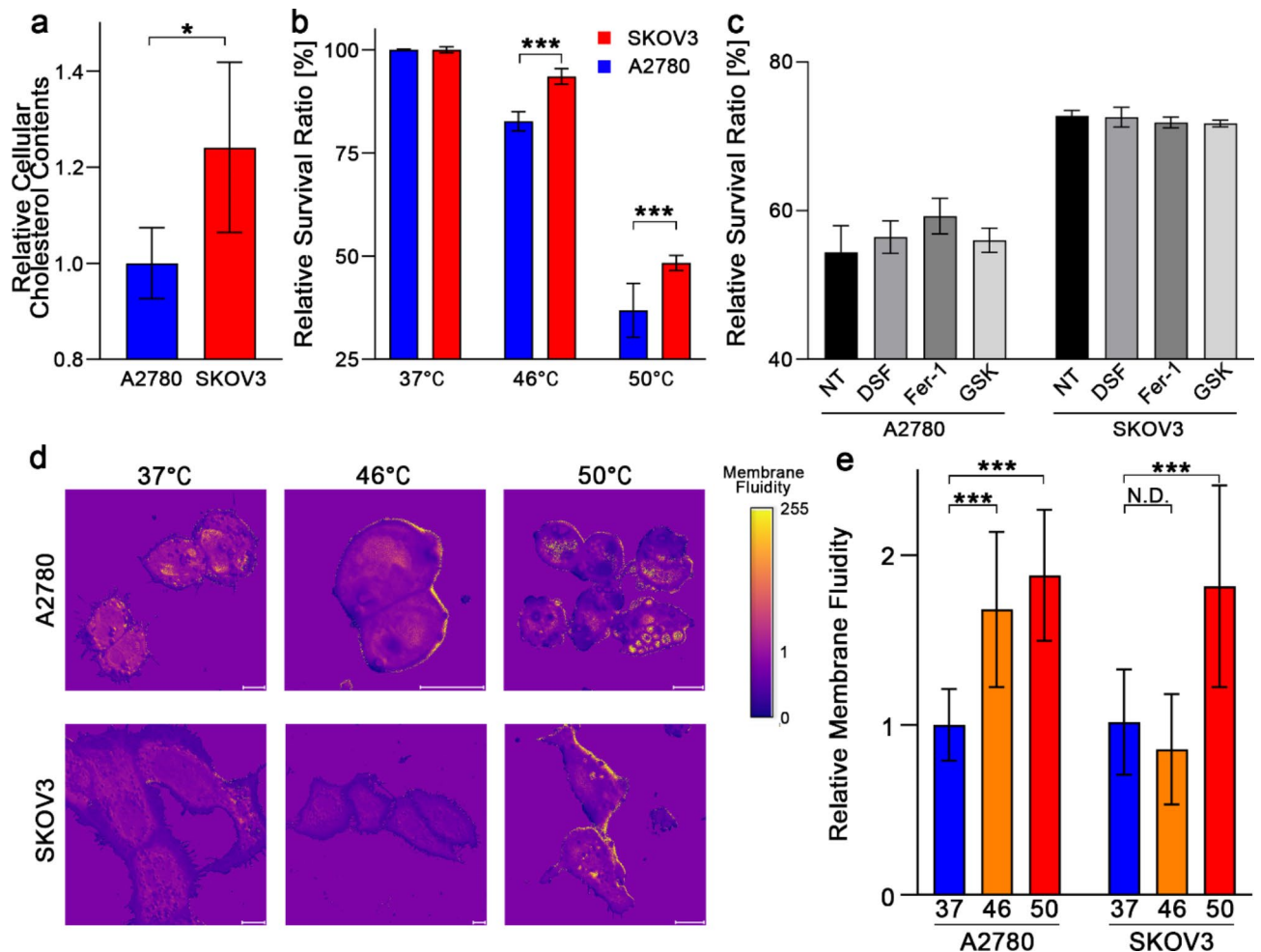
Fig. 2. Increase of membrane fluidity due to the temperature correlates with necrosis. (**a**) Relative cellular cholesterol contents of A2780 and SKOV3 cells. Mean ± S.D.; $n = 3$. Student's t test. *$P < 0.01$. (**b**) Relative survival ratios of A2780 and SKOV3 cells after heat shock for 1 h at indicated temperatures. Mean ± S.D.; $n = 3$. Student's t test. ***$P < 0.001$. (**c**) Relative survival ratios of A2780 and SKOV3 cells after heat shock for 1 h at 47 °C in the non-treated (NT) group and disulfiram (DSF)-, ferrostatin-1 (Fer-1)- and GSK-872 (GSK)-treated groups. (**d**) Membrane fluidity of A2780 and SKOV3 cells after heat shock for 1 h at indicated temperature. (**e**) Mean membrane fluidity of cells analyzed from (d) using the Image J software. Mean ± S.D.; $n = 15 \sim 20$. One-way Analysis of Variance (ANOVA). ***$P < 0.001$.

nuclear fluorescence were observed in both cell types. However, these events were noted even under non-heated conditions (Supplementary Fig. S3b and c), indicating that necrosis was independent of these changes. Under cholesterol-depleted conditions, both A2780 and SKOV3 cells showed complete disappearance of calcium and a significant decrease in nuclear fluorescence (Fig. 4c and d). In contrast to the heated cells, non-heated cells did not show this disappearance, even under cholesterol-depleted conditions (Supplementary Fig. S3d and e). These events were observed in all monitored cells (Fig. 4e-h). Under non-cholesterol-depleted conditions, only A2780 cells showed approximately 25% necrosis among all cells after 1 h. However, the A2780 and SKOV3 cells showed total necrosis after 55 min (Fig. 4i and j). This necrosis ratio was consistent with the results of the LT50 assay (Fig. 3b), confirming that the same cell death morphology was observed. Hence, increased membrane fluidity, resulting in necrosis due to membrane disruption, improved with cholesterol depletion.

Thermal resistance of cancer cells can be estimated based on cellular cholesterol contents

As demonstrated in A2780 and SKOV3 cells, cholesterol contributed to heat-induced necrosis resistance by suppressing the increase in membrane fluidity. To confirm that cholesterol functioned similarly in cells other than A2780 and SKOV3, we prepared the following cell types: human cancer cell lines, such as endometrial cancer cell lines Hec1-A and KLE and breast cancer cell lines MDA-MB-231 and MCF-7; and mouse cancer cell lines, such as colon cancer cell line MC38 and breast cancer cell lines MM48 and FM3A. We measured original cholesterol levels (Fig. 5a) and LT50 values (Fig. 5b) for each cell line. As expected, cholesterol and LT50 showed a certain correlation (Fig. 5c), supporting the hypothesis that high cholesterol levels render the induction of necrosis more difficult in A2780 and SKOV3 cells. In addition, cholesterol depletion in these cells significantly

reduced LT50s (Fig. 5d) regardless of the strength of the original thermal resistance. In addition, a reduction in thermal resistance was observed over a wide range of temperatures (Fig. 5e).

Cholesterol depletion amplifies the effects of hyperthermia in vivo

We investigated whether the reduction in thermal resistance due to cholesterol depletion could be recapitulated under in vivo conditions in tumor tissues. We treated mice subcutaneously implanted with SKOV3ip2 using HPβCD to deplete tumor cholesterol. We then evaluated the effects of hyperthermia on tumor growth inhibition. SKOV3ip2 cells established from the i.p. injection model showed thermal resistance similar to that observed with the original SKOV3 cells (Supplementary Fig. S4a and b). For hyperthermia, gold nanoparticles were locally administered near the tumor, and the tumor was heated using near-infrared light for 10 min (Fig. 6a). During heat shock, the temperature near the tumor was controlled at 50 ~ 55 °C using a thermal camera (Fig. 6b). HPβCD treatment depleted tumor cholesterol (Fig. 6c). To evaluate the therapeutic effect, we referred to the previous reports[22] and set a tumor size threshold of 100 mm^3. Based on this threshold, we calculated the response ratio, reflecting the percentage of mice with tumor sizes over the threshold at the end of the observation period. Compared to the NT and HPβCD groups, hyperthermia alone slightly delayed tumor growth; however, the final RR remained primarily unimproved (Fig. 6d). In contrast, combining hyperthermia with cholesterol depletion resulted in significant suppression of tumor growth (Fig. 6e). In addition, tumor disappearance was observed in most mice (Fig. 6f). The actual weight of the tumor tissue was also suppressed under combined conditions (Fig. 6g). These results indicate that the combination of cholesterol depletion and hyperthermia may be an effective treatment strategy for cancer.

Discussion

We showed that heat, as a simple physical stressor, induces cell death. Cell death morphological characteristics induced by heat stress have been examined previously. According to a previously reported classification, apoptotic cells include early-stage apoptosis cells[23-25]. Necrotic cells include necrosis cells[24,25], late-phase apoptosis cells[24,25], late-phase pyroptosis cells[15,26,27], late-phase ferroptosis[28-30], and necroptosis cells[27,30]. Programmed cell death, such as apoptosis[9,12], ferroptosis[31,32], necroptosis[33,34], and pyroptosis[35,36] is induced by heat shock. However, only a few reports mention necrosis-mediated cell death under heat shock[8]. The relationship between membrane fluidity and necrosis has been previously reported[37]. We hypothesized that an excessive increase in membrane fluidity directly disrupted the plasma membrane. This is the first study to show that heat-induced increases in membrane fluidity correlate with necrosis. In addition, our results indicated that necrosis and apoptosis occurred simultaneously at different time points after heat shock (Fig. 1a-c). Thus, heat shock-induced cell death is regulated by at least two independent mechanisms: early-phase death by necrosis and late-phase death by apoptosis (Fig. 7). The activation of energy metabolism in SKOV3 cells by intracellular metabolic adaptation prevents late-phase cell death after heat shock by sparing cells from energy depletion[6]. In this study, we showed that susceptibility to necrosis, an early-phase cell death induced after heat shock, is regulated by cholesterol-induced increases in membrane fluidity (Figs. 5d and 7). HSPs are heat-responsive proteins whose expression is induced after heat shock in both A2780 and SKOV3 cells. In addition, since the increase in HSP expression is noted several hours after stress induction[38], it is unlikely that it is highly correlated with necrosis resistance.

Cholesterol is known to regulate temperature-dependent changes in membrane fluidity and has been reported to suppress membrane fluidity at temperatures higher than the phase transition of lipids[39,40]. A bimodal phase transition temperature was observed in DMPC liposomes containing cholesterol, consistent with previous reports[41,42]. Cholesterol depletion using MβCD eliminated this bimodality (Supplementary Fig. S2a). This bimodality is attributed to the polarization of the DMPC membrane into the cholesterol-rich phase, L_o, and cholesterol-poor phase, L_β, each of which undergoes an independent phase transition (Supplementary Fig. S2b)[43]. MβCD may homogenize the membrane composition by cholesterol depletion and contribute to the temperature-dependent increase in the fluidity of the entire membrane structure. In biological membranes, cholesterol-rich regions, known as lipid rafts, are also formed[44], and MβCD has been reported to eliminate lipid rafts[45]. Based on the above, MβCD has been hypothesized to homogenize cholesterol in cell membranes, thereby promoting an increase in the whole membrane fluidity.

We observed a significant relationship between cholesterol levels and membrane fluidity (Fig. 3f). This indicates that not only cholesterol levels but also the activity of cholesterol synthesis can be used as biomarkers of hyperthermia sensitivity. In addition, if cholesterol levels are high, and cancer cells depict thermal resistance, cholesterol depletion may amplify the efficacy of hyperthermia. We confirmed that cholesterol depletion by treatment with HPβCD improved the therapeutic effect of hyperthermia. Some studies have attempted to treat cancer by depleting cholesterol using CD-based drugs[46-49]. There have been reports of cholesterol depletion suppressing the invasive potential of breast cancer cells, suggesting that cholesterol is an effective target in cancer treatment[49]. The results of this study indicate that cholesterol removal may be a useful treatment modality, not only on its own but also in combination with other therapies. However, because the combination of whole-body cholesterol depletion and whole-body hyperthermia may lead to adverse events, cancer tissue-selective cholesterol depletion and local hyperthermia are considered suitable for clinical applications. Therefore, in vivo experiments were conducted by combining the transient removal of cholesterol from cancer tissues via local administration with local hyperthermia treatment.

Typically, the therapeutic efficacy of hyperthermia involves two steps. Direct cell death is induced by heat shock. Next, anticancer immunity is activated by DAMPs released from cancer cells killed by hyperthermia[21]. In nude mice used for hyperthermia, immune activation cannot be expected owing to T cell deficiency. Hence, we demonstrated only the effects of cholesterol depletion and hyperthermia on cell death. In clinical cases, immune activation by the leakage of DAMPs is expected, indicating that our cholesterol depletion strategy has
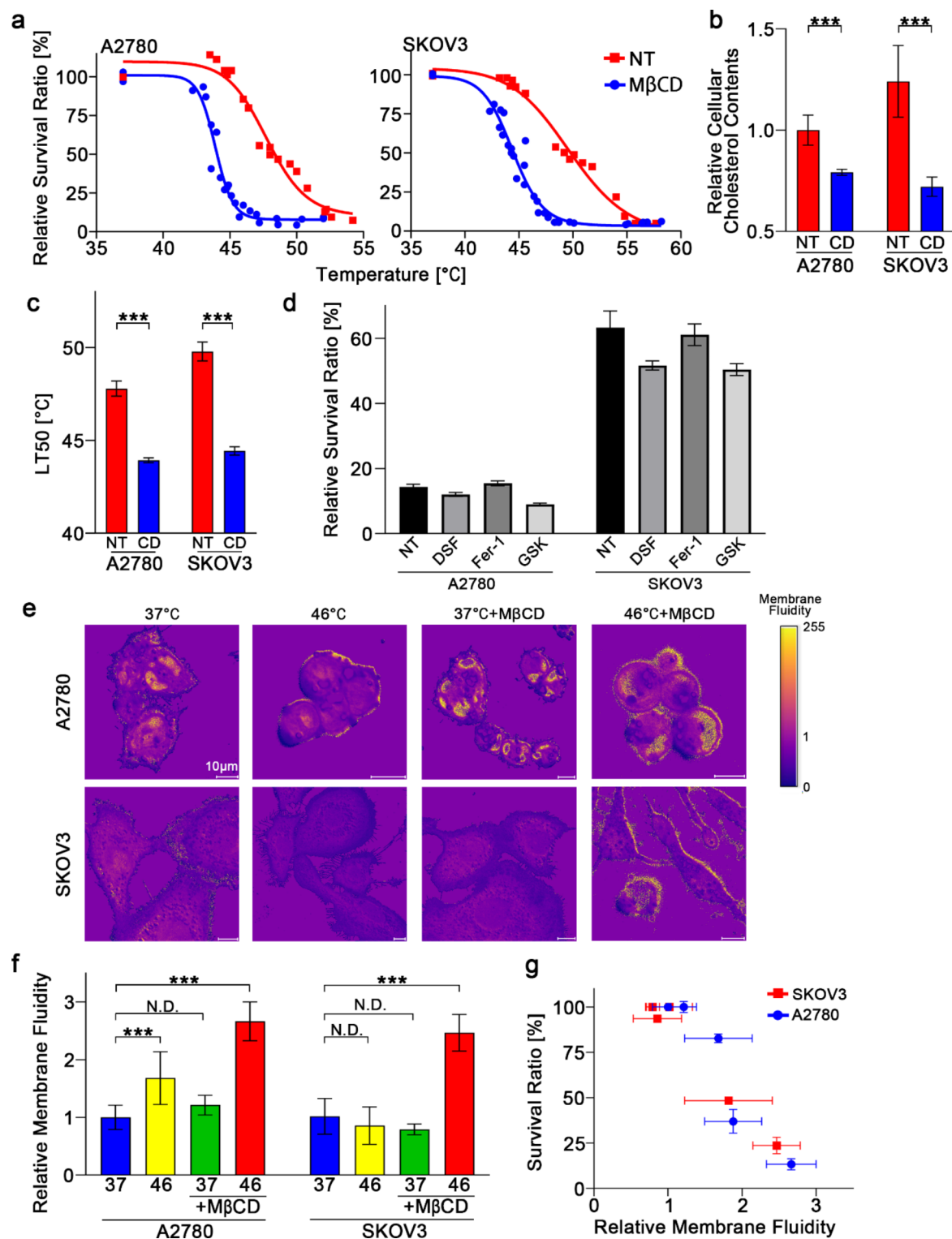
the potential to further contribute to improved response rates. Because cholesterol depletion primarily induces necrosis via heat shock, it is considered the potential strategy for the induction of the release of DAMPs[21].

Collectively, cholesterol contributes to thermal resistance by suppressing heat-induced necrosis and preventing heat-induced increase in membrane fluidity. Cholesterol depletion reduces thermal resistance and enhances the therapeutic effects of hyperthermia in thermally resistant cells.

Limitations of the study

We have shown that local administration of cholesterol-depleting drugs to tumors improves the depletion of cholesterol and the therapeutic efficacy of hyperthermia. However, in clinical practice, tumors often form deep in the body, such as in organs, and local administration of cholesterol depletion drugs leads to increased invasiveness.

◀ **Fig. 3**. Cholesterol depletion effect on membrane fluidity and survival ratio under heat shock. (**a**) Relative cell survival ratio after heat shock. A2780 and SKOV3 cells were heated for 1 h at the indicated temperature. The red and blue lines show survival ratios of non-treated and MβCD-treated cells, respectively. (**b**) Relative cellular cholesterol contents of A2780 and SKOV3 cells under non-cholesterol-depleted condition and cholesterol-depleted conditions. Mean ± S.D.; $n = 3$. Student's t test. ***$P < 0.01$. (**c**) LT50 values of A2780 and SKOV3 cells under MβCD treatment (CD) and non-treated (NT) conditions. Mean ± S.D.; $n = 20 \sim 26$. Student's t-test. ***$P < 0.001$. (**d**) Relative survival ratio of A2780 cells and SKOV3 cells after heat shock for 1 h at 44 °C in the non-treated (NT) group and disulfiram (DSF)-, ferrostatin-1 (Fer-1)-, and GSK-872 (GSK)-treated groups. A2780 and SKOV3 cells were treated with MβCD to deplete cholesterol. (**e**) Membrane fluidity of A2780 and SKOV3 cells after heat shock for 1 h at indicated temperature and condition. (**f**) Mean membrane fluidity of cells analyzed from (**e**) using the Image J software. Mean ± S.D.; $n = 15 \sim 20$. One-way Analysis of Variance (ANOVA). ***$P < 0.001$. (**g**) Distribution plot of relative survival ratios and relative membrane fluidity. Each plot represents the result of each condition for A2780 cells and SKOV3 cells. Relative survival ratio; Mean ± S.D.; $n = 3$. Relative membrane fluidity obtained from (B); Mean ± S.D.; $n = 15 \sim 20$.

Low molecular weight compounds such as MβCD and HPβCD, when administered intravenously, accumulate in organs such as the liver and spleen, where blood flow is high. Hence, a drug that can accumulate specifically in cancer cells and remove cholesterol in tumor tissue is acquired.

The use of cyclic molecules, such as rotaxane with enhanced cancer-accumulating capacity to encapsulate cholesterol-depleting drugs, may render the depletion of cholesterol from tumors through intravenous administration possible.

Method
Mice
The following BALBc/ nude mice was purchased from Japan SLC (Shizuoka, Japan). Mice were anesthetized with a triad of anesthesia consisting of domitor (Zenoaq, Fukushima, Japan), Midazolam (Nichi-Iko, Toyama, Japan), and Butorphanol (Meiji Animal Health, Kumamoto, Japan). Cervical dislocation was used for euthanasia. All animal procedures reported in this study were approved by the Ethics Committee of Chiba university (CA 6–96). All animal experiments were conducted in accordance with Chiba university regulations for the implementation of animal experiments. All animal reporting was conducted in accordance with ARRIVE guidelines 2.0[50].

Cell culture
The human ovarian cancer cell line A2780 was purchased from the European Collection of Authenticated Cell Culture (ECACC, Salisbury, UK). SKOV3, KLE, MDA-MB-231, and MCF7 were purchased from the American Type Culture Collection (ATCC, Manassas, Virginia, USA). Hec1-A was purchased from the Japanese Collection of Research Bioresources (JCRB, Osaka, Japan). The mouse cancer cell line MM48 was purchased from the Cell Resource Center at Tohoku University. MC38 was purchased from Kerafast (Shirley, Massachusetts, USA). FM3A was purchased from JCRB. Cells were cultured in RPMI 1640 (Nacalai Tesque, Tokyo, Japan) or D-MEM high glucose (Nacalai Tesque) supplemented with 10% fetal bovine serum (FBS; Nichirei, Tokyo, Japan) and 1% penicillin and streptomycin (Nacalai Tesque) in 5% CO_2 at 37 °C.

Establishment of SKOV3 ip2 cells
BALBc/ nude mice (five weeks old, female, SLC, Shizuoka, Japan) were intraperitoneally (i.p.) inoculated with SKOV3 cells. After tumors were collected from the intraperitoneal cavity, the tissue was dissociated into cells with a tumor dissociation kit (Myltenyi Biotec, Bergisch Gladbach, Germany) according to the manufacturer's suggestions. Briefly, the tissue was separated into small lumps and incubated with an enzyme mix solution. Subsequently, small lumps were dissociated into cells by filtering using a cell strainer. The resulting cells were known as SKOV3ip1. SKOV3ip1 cells were cultured in an RPMI 1640 complete medium. BALBc/ nude mice (female, five weeks old, SLC) were i.p. inoculated with SKOV3ip1. SKOV3ip2 cells were obtained by repeating the aforementioned procedure.

Treatment of Cancer cells with heat shock
Cells were seeded in 6-cm dishes (2 to 4×10^5 cells/3 ml of culture medium) or 10-cm dishes (1 to 1.5×10^6 cells/10 ml of culture medium). The cells were heated in a cell culture chamber (C-140 A, Blast, Kawasaki, Japan) for 1 h at indicated temperatures that were measured with a thermal imaging camera (E6, FLIR, Wilsonville, Oregon, USA), followed by incubation at 37 °C in a regular cell culture incubator. In the cell death inhibition experiment, cells were incubated for 3 h with 20 μM disulfiram (DSF) (Selleck Biotechnology, Kanagawa, Japan), 20 μM ferrostatin-1 (Fer-1) (Selleck Biotechnology), and 25 μM GSK-872 (GSK) (Selleck Biotechnology) followed by heat shock.

Depletion of cholesterol from Cancer cells
Just before the heat shock, the cell culture medium was replaced with RPMI1640 with or without 2.5 mM Methyl-beta-cyclodextrin (MβCD; Tokyo Chemical industry, Tokyo, Japan). Cells were exposed to MβCD during heat shock and used for the subsequent experiments.
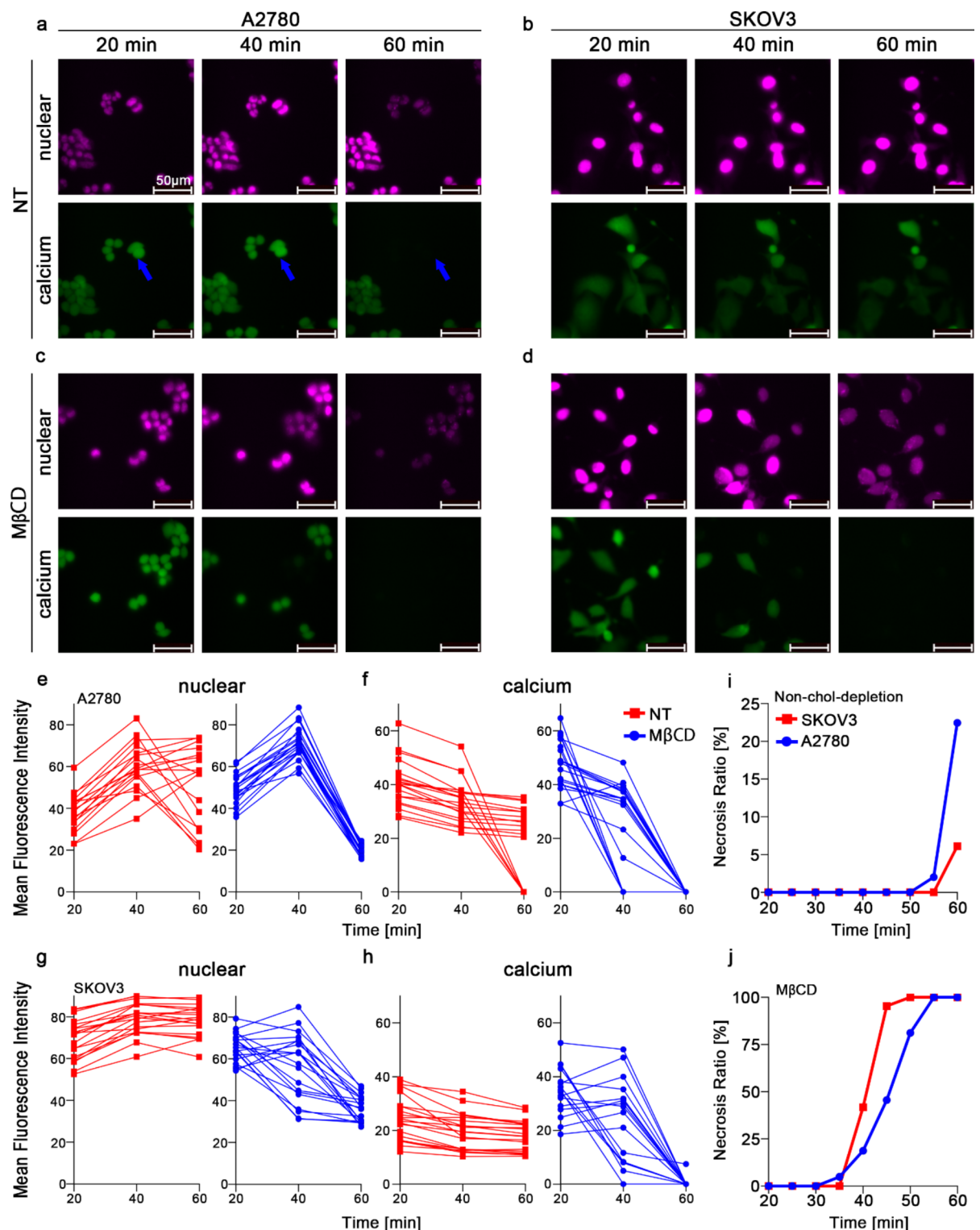
Fig. 4. Real-time imaging of cholesterol non-depleted cells and depleted cells under heat shock.   (**a-d**) Real-time imaging of A2780 and SKOV3 cells with or without cholesterol depletion under heat shock. A2780 and SKOV3 cells were heated for 1 h at approximately 46°C. Cellular calcium and nuclear levels were monitored every 5 min. Images captured at 20 min, 40 min, and 60 min are shown. The blue arrow points at representative necrosis cells in A2780 group. (**e-h**) Mean fluorescence intensity (MFI) of the nuclear and calcium in A2780 and SKOV3 cells under heat shock. The MFI was calculated by tracking each cell in (**a-d**). The blue and red lines show results with and without MβCD treatment, respectively. (**i** and **j**) Total necrosis ratio of non-cholesterol-depleted cells (**i**) and cholesterol-depleted cells (**j**) under heat shock calculated from real-time images. The blue and red lines show result of A2780 and SKOV3 cells, respectively.
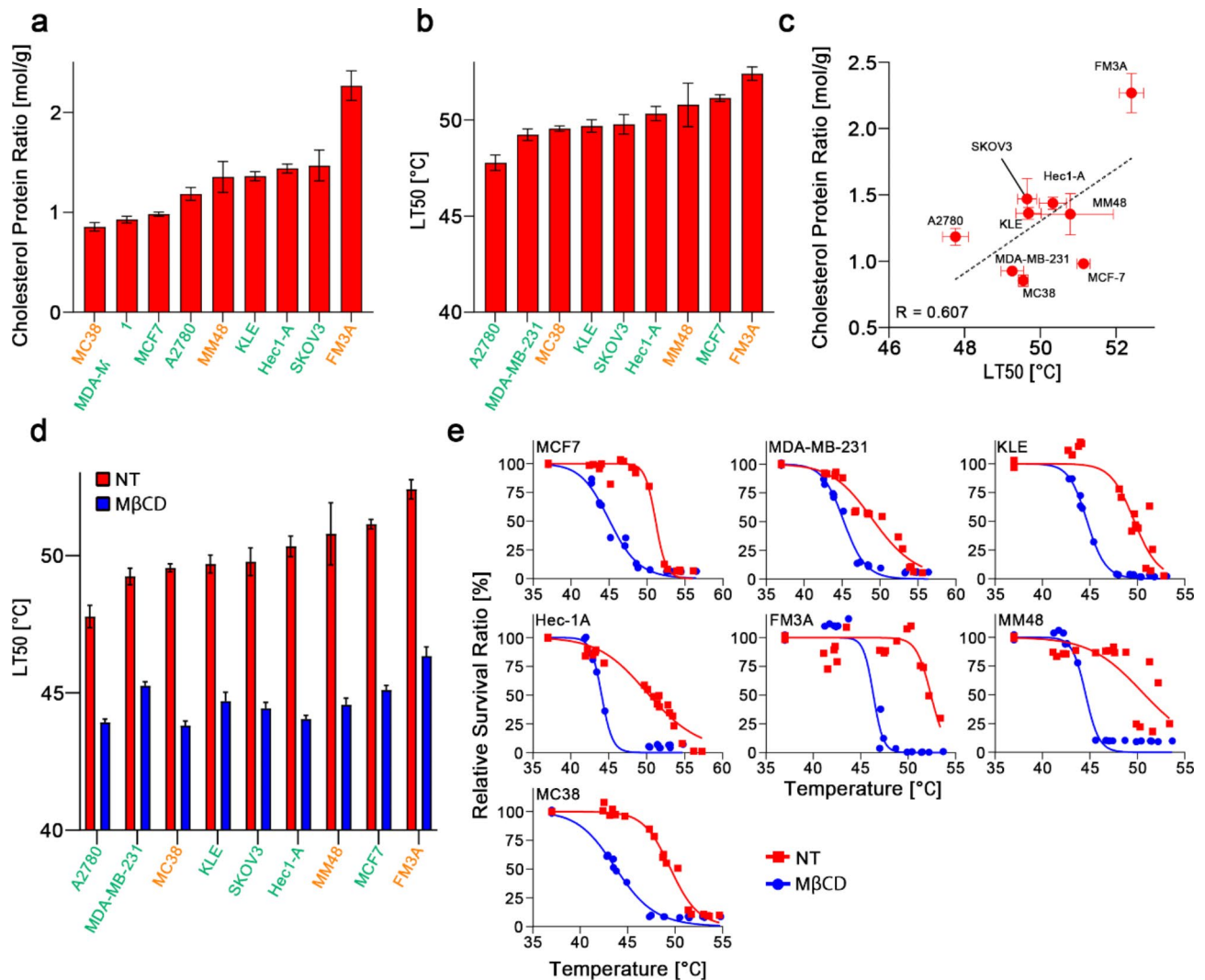
Fig. 5. Cholesterol contents and thermal resistance are partially correlated. (**a**) Original cellular cholesterol/protein ratio of each cell line. Orange and green indicate mouse and human cell lines, respectively. Mean ± S.E.; $n = 3 \sim 4$. (**b**) LT50 values of each cell line. Orange and green indicate represent mouse and human cell lines, respectively. Mean ± S.E.; $n = 20 \sim 26$. (**c**) Dot plot of the cholesterol/protein ratio and LT50 values under non-cholesterol-depleted conditions. The dotted line shows the linear approximation of all cell lines. The correlation coefficients are shown in the lower left panel of the plot. (**d**) The LT50 value of each cell line. The red and blue bars indicate MβCD treatment and untreated conditions, respectively. Orange and green represent mouse and human cell lines, respectively. Mean ± S.E.; $n = 20 \sim 26$. (**e**) Relative survival ratios of human and mouse cancer cell lines immediately after heat shock at the indicated temperatures. Survived cells were detected by the MTT assay. The red and blue lines show the results for non-cholesterol-depleted and cholesterol-depleted conditions, respectively.

Flow cytometric evaluation of cell death morphology

Heated cells and non-heated cells were washed and detached using trypsin-ethylenediaminetetraacetic acid (EDTA). The cell pellets were washed twice with 1 ml of phosphate-buffered saline (PBS; Nissui Pharmaceutical, Tokyo, Japan). After centrifuging the cells and removing the supernatant, pellets were suspended with 200 μL of Annexin binding buffer (Becton Dickinson, Franklin Lakes, New Jersey, USA). The suspension was passed through a 48-μm nylon mesh (Tokyo Garasu Kikai, Tokyo, Japan) to obtain a single-cell suspension. Cells were dyed with DAPI (BioLegend, San Diego, California, USA) and AnnexinV-FITC (Becton Dickinson) to detect apoptosis and necrosis. DAPI was detected with the excitation and emission wavelengths of 405 nm and 450 nm and Annexin V-FITC at 488 nm and 530 nm, respectively, using a FACSCanto™ II (Becton Dickinson). Analysis was performed using the FlowJo™ software (Becton Dickinson).

Real-time imaging of Cancer cells under heat shock

Cells were seeded in six-well plates (0.1 to 0.3×10^6 cells/2 ml of culture medium). Cells were heated in a stage top incubator (STRG-KIW, Tokai hit, Shizuoka, Japan) for 1 h at 46°C. Under heat shock, cells were monitored
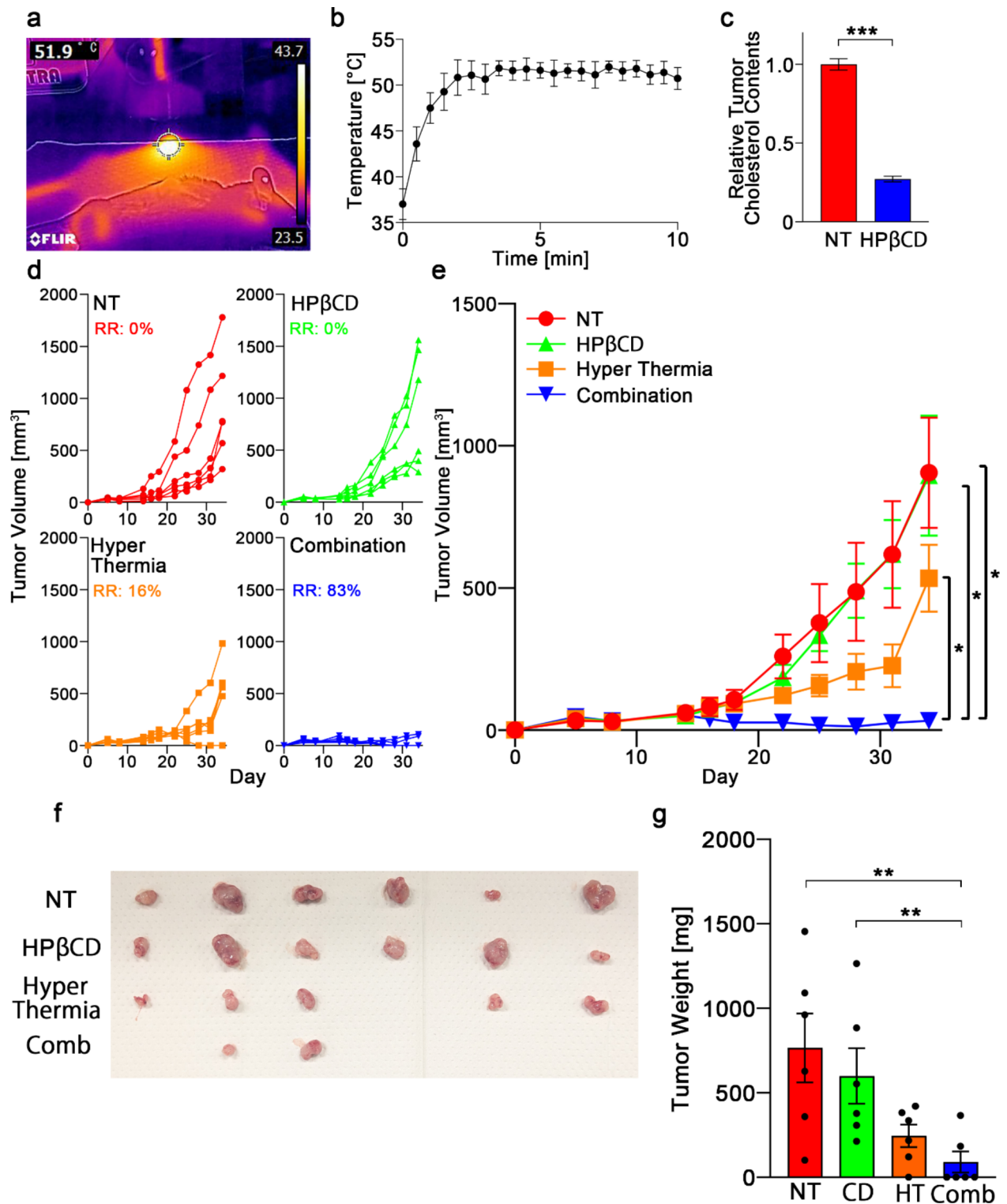
Fig. 6. Cholesterol depletion amplified hyperthermia effect. (**a**) Representative thermal camera image during the hyperthermia. (**b**) Temperature of the tumor surface determined using (**a**). The temperature was monitored every 30 s and maintained at approximately 50 ~ 55 °C. Mean ± S.D.; $n = 12$. (**c**) Cholesterol levels of tumor tissue cells under non-cholesterol-depleted (NT) and cholesterol-depleted (HPβCD) conditions. Mean ± S.D.; $n = 3$. Student's t test. ***$P < 0.001$. (**d**) Tumor growth in individual mice under non-treated (NT: red), cholesterol-depletion only (HPβCD: green), hyperthermia only (hyperthermia: orange), and a combination of cholesterol-depletion and hyperthermia (Combination: blue) conditions. The response rate (RR) of each treatment is shown in respective colors. (**e**) Average tumor growth after each treatment. Mean ± S.E.; $n = 6$. One-way Analysis of Variance (ANOVA). *$P < 0.05$. (**f**) Actual tumor tissues were collected from subcutaneous tumors under each condition. The blank area indicates tumor disappearance after treatment. (g) Weight of the tumor tissue collected subcutaneously. Mean ± S.E.; $n = 6$. One-way Analysis of Variance (ANOVA). **$P < 0.01$.
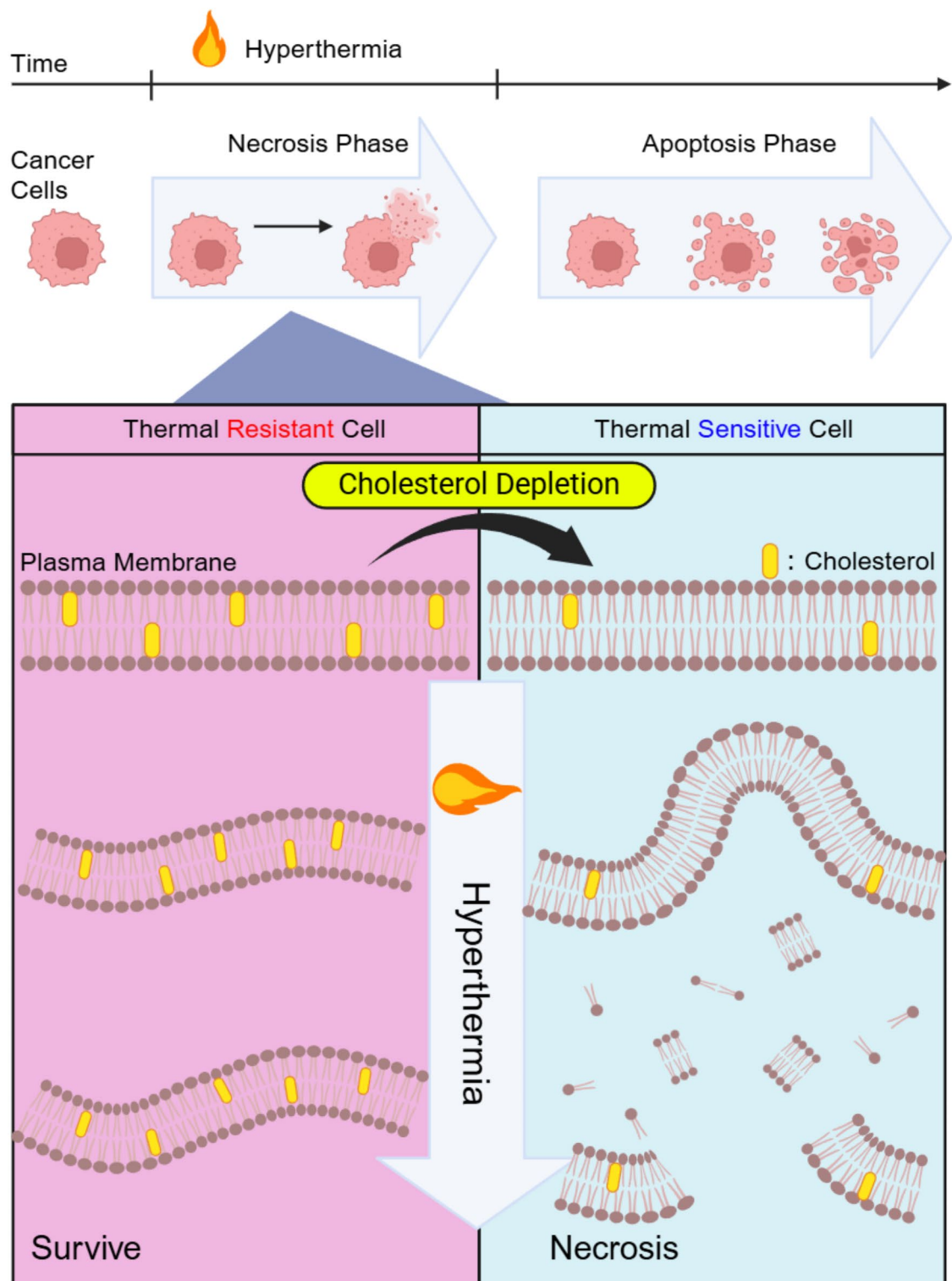
Fig. 7. Regulation of cell death morphology by thermal stimulation, and cholesterol-induced membrane fluidity and necrosis. Heat shock-induced cell death is broadly classified into two types, early necrosis and late apoptosis. They each have their own independent control mechanisms. In necrosis, heat-induced enhancement of membrane fluidity is suppressed by cholesterol, preventing membrane disruption. Thus, cholesterol-rich cells are resistant to heat-induced necrosis. Cholesterol depletion is the way to convert thermal resistant cells into sensitive cells.

using BZX-810 (Keyence, Tokyo, Japan) every 5 min. The cells were dyed with calcein-AM (Nacalai Tesque) and DRAQ5 (AAT Bioquest, Pleasanton, California, USA). Calcein-AM was detected with the excitation and emission wavelengths of 488 and 530 nm and DRAQ5 at 643 nm and 670 nm, respectively. The fluorescence intensity of each cell was measured using ImageJ[51–53] and TrackMate-Cellpose plugin.

Cell membrane fluidity analysis after heat shock
Cells were dyed using LipiORDER (Funakoshi, Tokyo, Japan). LipiORDER was detected using a single excitation wavelength of 405 nm and two emission wavelengths of 510 and 575 nm using STELLARIS 5 (Leica, Wetzlar, Germany). The pseudo-color images were generated and analyzed using the ImageJ software and Ratio-plus plugin.

Survival ratio analysis
To detect living cells, cells were treated with 3-(4,5-Dimethyl-2-thiazolyl)-2,5-diphenyltetrazolium Bromide reagent (MTT; Fujifilm, Tokyo, Japan). After 1 h of incubation, the MTT crystals were eluted using dimethyl sulfoxide (DMSO; Nacalai Tesque). The absorbance of MTT was determined with Spectra Max i3 (Molecular Device, Sunnyvale, California, USA). The calculation of LT50s and curve fitting were performed using GraphPad Prism 10 (San Diego, California, USA).

Measurement of cholesterol contents
To extract cholesterol, tissues were homogenized using Shake Master Neo (Bio-Medical Science, Tokyo, Japan), and cultured cells were suspended in the acetic acid solution. Cholesterol was extracted using the Folch method[54]. Briefly, cholesterol was recovered from the chloroform layer after mixing the methanol-chloroform (1:2) mixture and the homogenized solution. Total cholesterol content was measured using the Amplite Cholesterol Quantitation Kit (AAT Bioquest, Pleasanton, California, USA).

Preparation of gold nanorods
Gold nanorods were purchased from Dai Nippon Toryo Co. LTD. (Osaka, Japan). To remove excess cetyltrimethylammonium bromide (CTAB), which was used as a stabilizer in the suspension, the gold nanorods were centrifuged at $12,000 \times g$ for 10 min and resuspended in water (two cycles). Subsequently, gold nanorods were modified using thiol-terminated polyethylene glycol (SH-PEG, MW 5,000 Da) to improve their biocompatibility and stability. The SH-PEG was added to the gold nanorod suspension at a PEG/gold molar ratio of 1.5, and the suspension was stirred overnight at room temperature. To remove unreacted SH-PEG, a dialysis membrane (MWCO 12,000 Da) was used. and the dialysis water was changed thrice daily.

In vivo hyperthermia treatment
BALB/c nude mice (female, five weeks old, SLC) were subcutaneously (s.c.) inoculated with SKOV3 ip2 (4.0×10^6 cells/mouse). When tumor volume reached $40 \sim 50$ mm[3], hydroxypropyl-beta-cyclodextrin (HPβCD; Tokyo Chemical industry, Tokyo, Japan) administration was initiated. A total of 30 mg/kg HPβCD or PBS was locally injected into the s.c. tumor thrice every two days. The next day after the first administration and third administration, hyperthermia was induced. Briefly, 4 μg of gold nanoparticles were locally injected into the tumor of each mouse, and then the tumor was heated using near-infrared light (NIR, $800 \sim 950$ nm) irradiation using MAX-303 (Asahi Spectra, Tokyo, Japan) for 10 min at approximately 53°C. The temperature around the tumor was monitored every 30 s using a thermal imaging camera (E6, FLIR).

Statistical analysis
All data are presented as the mean value $\pm$ S.E. Pair-wise comparisons were performed using Student's t-tests. Comparisons between multiple treatments were made using a one-way analysis of variance (ANOVA), followed by an appropriate post hoc test. P-values (both sides) were considered significant if less than 0.05. Statistical analyses were performed using the GraphPad Prism 10 software (GraphPad, Massachusetts, Boston, UA).

Data availability
The datasets generated during and analyzed during the current study are available from the corresponding author on reasonable request.

References
1. Chichel, A., Skowronek, J., Kubaszewska, M. & Kanikowski, M. Hyperthermia – description of a method and a review of clinical applications. *Rep. Practical Oncol. Radiotherapy*. **12**, 267–275 (2007).
2. Nguyen, H. T., Tran, K. K., Sun, B. & Shen, H. Activation of inflammasomes by tumor cell death mediated by gold nanoshells. *Biomaterials* **33**, 2197–2205. https://doi.org/10.1016/j.biomaterials.2011.11.063 (2012).
3. Ahmed, A. A. & Tait, S. W. G. Targeting Immunogenic cell death in cancer. *Mol. Oncol.* **14**, 2994–3006. https://doi.org/10.1002/1878-0261.12851 (2020).
4. Adkins, I., Fucikova, J., Garg, A., Agostinis, D. & Špíšek, R. Physical modalities inducing Immunogenic tumor cell death for cancer immunotherapy. *Oncoimmunology* **3**, e968434. https://doi.org/10.4161/21624011.2014.968434 (2014).
5. van Driel, W. J., Koole, S. N. & Sonke, G. S. Hyperthermic intraperitoneal chemotherapy in ovarian Cancer. *N Engl. J. Med.* **378**, 1363–1364. https://doi.org/10.1056/NEJMc1802033 (2018).
6. Kanamori, T. et al. Investigation of energy metabolic dynamism in hyperthermia-resistant ovarian and uterine cancer cells under heat stress. *Sci. Rep.* **11**, 14726. https://doi.org/10.1038/s41598-021-94031-9 (2021).

7. Hatakeyama, H. et al. Role of CTGF in sensitivity to hyperthermia in ovarian and uterine cancers. *Cell. Rep.* **17**, 1621–1631. https://doi.org/10.1016/j.celrep.2016.10.020 (2016).

8. Li, S., Chien, S. & Brånemark, P. I. Heat shock-induced necrosis and apoptosis in osteoblasts. *J. Orthop. Res.* **17**, 891–899. https://doi.org/10.1002/jor.1100170614 (1999).

9. Kassis, S., Grondin, M. & Averill-Bates, D. A. Heat shock increases levels of reactive oxygen species, autophagy and apoptosis. *Biochim. Biophys. Acta Mol. Cell. Res.* **1868**, 118924. https://doi.org/10.1016/j.bbamcr.2020.118924 (2021).

10. Kobayashi, T. Cancer hyperthermia using magnetic nanoparticles. *Biotechnol. J.* **6**, 1342–1347. https://doi.org/10.1002/biot.20110 0045 (2011).

11. Pallepati, P. & Averill-Bates, D. A. Activation of ER stress and apoptosis by hydrogen peroxide in HeLa cells: Protective role of mild heat preconditioning at 40°C. *Biochim. Biophys. Acta.* **1813**, 1987–1999. https://doi.org/10.1016/j.bbamcr.2011.07.021 (2011).

12. Li, L. et al. Heat stress induces apoptosis through a Ca^{2+}-mediated mitochondrial apoptotic pathway in human umbilical vein endothelial cells. *PLoS One.* **9**, e111083. https://doi.org/10.1371/journal.pone.0111083 (2014).

13. Gu, Z. T. et al. Heat stress induced apoptosis is triggered by transcription-independent p53, Ca(2+) dyshomeostasis and the subsequent Bax mitochondrial translocation. *Sci. Rep.* **5**, 11497. https://doi.org/10.1038/srep11497 (2015).

14. Gu, Z. T. et al. Heat stress induces apoptosis through transcription-independent p53-mediated mitochondrial pathways in human umbilical vein endothelial cell. *Sci. Rep.* **4**, 4469. https://doi.org/10.1038/srep04469 (2014).

15. Fink, S. L. & Cookson, B. T. Apoptosis, pyroptosis, and necrosis: mechanistic description of dead and dying eukaryotic cells. *Infect. Immun.* **73**, 1907–1916. https://doi.org/10.1128/IAI.73.4.1907-1916.2005 (2005).

16. Janus, P. et al. Pro-death signaling of cytoprotective heat shock factor 1: Upregulation of NOXA leading to apoptosis in heat-sensitive cells. *Cell. Death Differ.* **27**, 2280–2292. https://doi.org/10.1038/s41418-020-0501-8 (2020).

17. WARBURG, O. On the origin of cancer cells. *Science* **123**, 309–314. https://doi.org/10.1126/science.123.3191.309 (1956).

18. Warburg, O., Wind, F., & Negelein, E., The metabolism of & tumors in the body. *J. Gen. Physiol.* **8**, 519–530 https://doi.org/10.108 5/jgp.8.6.519 (1927).

19. Schlesinger, M. J. Heat shock proteins. *J. Biol. Chem.* **265**, 12111–12114 (1990).

20. Janko, C. et al. Navigation to the graveyard-induction of various pathways of necrosis and their classification by flow cytometry. *Methods Mol. Biol.* **1004**, 3–15. https://doi.org/10.1007/978-1-62703-383-1_1 (2013).

21. Murao, A., Aziz, M., Wang, H., Brenner, M. & Wang, P. Release mechanisms of major damps. *Apoptosis* **26**, 152–162. https://doi.o rg/10.1007/s10495-021-01663-3 (2021).

22. Kurino, T. et al. Poor outcome with anti-programmed death-ligand 1 (PD-L1) antibody due to poor Pharmacokinetic properties in PD-1/PD-L1 blockade-sensitive mouse models. *J. Immunother Cancer.* https://doi.org/10.1136/jitc-2019-000400 (2020).

23. Vitale, I. et al. Apoptotic cell death in disease-Current Understanding of the NCCD 2023. *Cell. Death Differ.* **30**, 1097–1154. https://doi.org/10.1038/s41418-023-01153-w (2023).

24. Poon, I. K., Hulett, M. D. & Parish, C. R. Molecular mechanisms of late apoptotic/necrotic cell clearance. *Cell. Death Differ.* **17**, 381–397. https://doi.org/10.1038/cdd.2009.195 (2010).

25. Brauchle, E., Thude, S., Brucker, S. Y. & Schenke-Layland, K. Cell death stages in single apoptotic and necrotic cells monitored by Raman microspectroscopy. *Sci. Rep.* **4**, 4698. https://doi.org/10.1038/srep04698 (2014).

26. Shi, J., Gao, W., Shao, F. & Pyroptosis Gasdermin-Mediated programmed necrotic cell death. *Trends Biochem. Sci.* **42**, 245–254. https://doi.org/10.1016/j.tibs.2016.10.004 (2017).

27. Frank, D. & Vince, J. E. Pyroptosis versus necroptosis: Similarities, differences, and crosstalk. *Cell. Death Differ.* **26**, 99–114. https://doi.org/10.1038/s41418-018-0212-6 (2019).

28. Riegman, M. et al. Ferroptosis occurs through an osmotic mechanism and propagates independently of cell rupture. *Nat. Cell. Biol.* **22**, 1042–1048. https://doi.org/10.1038/s41556-020-0565-1 (2020).

29. Li, J. Y., Yao, Y. M., Tian, Y. P. & Ferroptosis A trigger of Proinflammatory state progression to immunogenicity in necroinflammatory disease. *Front. Immunol.* **12**, 701163. https://doi.org/10.3389/fimmu.2021.701163 (2021).

30. Costigan, A., Hollville, E. & Martin, S. J. Discriminating between apoptosis, necrosis, necroptosis, and ferroptosis by microscopy and flow cytometry. *Curr. Protoc.* **3**, e951. https://doi.org/10.1002/cpz1.951 (2023).

31. Yang, H. et al. Heat stress induces ferroptosis of Porcine Sertoli cells by enhancing CYP2C9-Ras- JNK axis. *Theriogenology* **215**, 281–289. https://doi.org/10.1016/j.theriogenology.2023.11.027 (2024).

32. Xu, J., Wang, X. L., Zeng, H. F. & Han, Z. Y. Methionine alleviates heat stress-induced ferroptosis in bovine mammary epithelial cells through the Nrf2 pathway. *Ecotoxicol. Environ. Saf.* **256**, 114889. https://doi.org/10.1016/j.ecoenv.2023.114889 (2023).

33. Zhou, J. et al. Heat stress-induced intestinal epithelial cells necroptosis via TLR3-TRIF-RIP3 pathway was dependent on p53. *Int. Immunopharmacol.* **122**, 110574. https://doi.org/10.1016/j.intimp.2023.110574 (2023).

34. Huang, W. et al. Heat stress induces RIP1/RIP3-dependent necroptosis through the MAPK, NF-κB, and c-Jun signaling pathways in pulmonary vascular endothelial cells. *Biochem. Biophys. Res. Commun.* **528**, 206–212. https://doi.org/10.1016/j.bbrc.2020.04.150 (2020).

35. Pei, Y., Geng, Y. & Su, L. Pyroptosis of HUVECs can be induced by heat stroke. *Biochem. Biophys. Res. Commun.* **506**, 626–631. https://doi.org/10.1016/j.bbrc.2018.10.051 (2018).

36. Deng, Q. F. et al. Heat stroke induces pyroptosis in spermatogonia via the cGAS-STING signaling pathway. *Physiol. Res.* **73**, 117–125. https://doi.org/10.33549/physiolres.935163 (2024).

37. Ros, U., Pedrera, L. & Garcia-Saez, A. J. Partners in crime: the interplay of proteins and membranes in regulated necrosis. *Int. J. Mol. Sci.* https://doi.org/10.3390/ijms21072412 (2020).

38. Tang, D. et al. Expression of heat shock proteins and heat shock protein messenger ribonucleic acid in human prostate carcinoma in vitro and in tumors in vivo. *Cell. Stress Chaperones.* **10**, 46–58. https://doi.org/10.1379/csc-44r.1 (2005).

39. McMullen, T. P., Vilchèze, C., McElhaney, R. N. & Bittman, R. Differential scanning calorimetric study of the effect of sterol side chain length and structure on dipalmitoylphosphatidylcholine thermotropic phase behavior. *Biophys. J.* **69**, 169–176. https://doi.o rg/10.1016/S0006-3495(95)79887-3 (1995).

40. Wu, E. S., Jacobson, K. & Papahadjopoulos, D. Lateral diffusion in phospholipid multibilayers measured by fluorescence recovery after photobleaching. *Biochemistry* **16**, 3936–3941. https://doi.org/10.1021/bi00636a034 (1977).

41. Serro, A. P. et al. Effect of Tetracaine on DMPC and DMPC + cholesterol biomembrane models: liposomes and monolayers. *Colloids Surf. B Biointerfaces.* **116**, 63–71. https://doi.org/10.1016/j.colsurfb.2013.12.042 (2014).

42. Mabrey, S., Mateo, P. L. & Sturtevant, J. M. High-sensitivity scanning calorimetric study of mixtures of cholesterol with dimyristoyl- and dipalmitoylphosphatidylcholines. *Biochemistry* **17**, 2464–2468. https://doi.org/10.1021/bi00605a034 (1978).

43. Hasan, I. Y. & Mechler, A. Cholesterol rich domains identified in unilamellar supported biomimetic membranes via Nano-Viscosity measurements. *Anal. Chem.* **88**, 5037–5041. https://doi.org/10.1021/acs.analchem.6b01045 (2016).

44. Gaus, K. et al. Visualizing lipid structure and raft domains in living cells with two-photon microscopy. *Proc. Natl. Acad. Sci. U S A.* **100**, 15554–15559. https://doi.org/10.1073/pnas.2534386100 (2003).

45. Larbi, A. et al. Effects of methyl-beta-cyclodextrin on T lymphocytes lipid rafts with aging. *Exp. Gerontol.* **39**, 551–558. https://doi .org/10.1016/j.exger.2003.10.031 (2004).

46. Saha, S. T. et al. 2-Hydroxypropyl-β-cyclodextrin (HPβCD) as a potential therapeutic agent for breast Cancer. *Cancers (Basel).* https://doi.org/10.3390/cancers15102828 (2023).

47. Ganjali Koli, M. & Fogolari, F. Exploring the role of cyclodextrins as a cholesterol scavenger: A molecular dynamics investigation of conformational changes and thermodynamics. *Sci. Rep.* **13**, 21765. https://doi.org/10.1038/s41598-023-49217-8 (2023).

48. Maja, M. & Tyteca, D. Alteration of cholesterol distribution at the plasma membrane of cancer cells: from evidence to pathophysiological implication and promising therapy strategy. *Front. Physiol.* **13**, 999883. https://doi.org/10.3389/fphys.2022.999883 (2022).
49. Maja, M. et al. Targeting cholesterol impairs cell invasion of all breast cancer types. *Cancer Cell. Int.* **24**, 27. https://doi.org/10.1186/s12935-023-03206-z (2024).
50. du Percie, N. et al. The ARRIVE guidelines 2.0: Updated guidelines for reporting animal research. *PLoS Biol.* **18**, e3000410. https://doi.org/10.1371/journal.pbio.3000410 (2020).
51. Schneider, C. A., Rasband, W. S. & Eliceiri, K. W. NIH image to imageJ: 25 years of image analysis. *Nat. Methods.* **9**, 671–675. https://doi.org/10.1038/nmeth.2089 (2012).
52. Rasband, W. S. *ImageJ, U.S. National Institutes of Health, Bethesda, Maryland, USA*, (1997). https://imagej.nih.gov/ij/.
53. Abramoff, M. D., Magalhaes, P. J. & Ram, S. J. Image processing with ImageJ. *Biophotonics Int.* **11**, 36–42 (2004).
54. Folch, J., Lees, M., & Sloane Stanley, G. H. A Simple method for the isolation and purification of total lipides from animal tissues. *J. Biol. Chem.* **226**, 497–509 (1957).

Acknowledgements

Author contributions

Conceptualization: T.K. and H.H.; data curation: T.K., S.Y., R.D., M.O., M.A. and T.F.; formal analysis: T.K.; funding acquisition: T.K. and H.H.; investigation: T.K. and H.H.; methodology: T.K. and H.H; project administration: H.H.; resources: K.H., R.T., W.X. and T.N.; software: T.K.; supervision: H.H., K.H., W.X., T.N.; validation: T.K.; visualization: T.K.; writing – original draft: T.K.; writing – review & editing: H.H.

Declarations

Competing interests

The authors declare no competing interests.

Additional information

Supplementary Information The online version contains supplementary material available at https://doi.org/10.1038/s41598-025-92232-0.

Correspondence and requests for materials should be addressed to H.H.

Reprints and permissions information is available at www.nature.com/reprints.

Publisher's note Springer Nature remains neutral with regard to jurisdictional claims in published maps and institutional affiliations.